ACS APPLIED MATERIALS & INTERFACES

Research Article

www.acsami.org

Covalent Entrapment of Cobalt–Iron Sulfides in N-Doped Mesoporous Carbon: Extraordinary Bifunctional Electrocatalysts for Oxygen Reduction and Evolution Reactions

Mengxia Shen,[†,‡] Changping Ruan,[†,‡] Yan Chen,[†,‡] Chunhuan Jiang,[†] Kelong Ai,*[,†] and Lehui Lu*[,†]

[†]State Key Laboratory of Electroanalytical Chemistry, Changchun Institute of Applied Chemistry, Chinese Academy of Sciences, Changchun, 130022, P. R. China

[‡]University of Chinese Academy of Sciences, Beijing, 100039, P. R. China

Supporting Information

ABSTRACT: To alleviate the kinetic barriers associated with ORR (oxygen reduction reaction) and OER (oxygen evolution reaction) in electrochemical systems, efficient nonprecious electrocatalysts are urgently required. Here we report a facile soft-template mediated approach for fabrication of nanostructured cobalt–iron double sulfides that are covalently entrapped in nitrogen-doped mesoporous graphitic carbon ($Co_{0.5}Fe_{0.5}S$@N-MC). Notably, with a positive half-wave potential (0.808 V) and a high diffusion-limiting current density, the composite material delivers unprecedentedly striking ORR electrocatalytic activity among recently reported nonprecious late transition metal chalcogenide materials in alkaline medium. Various characterization techniques, including X-ray absorption spectroscopy, X-ray photoelectron spectroscopy, and X-ray diffraction, are conducted to elucidate the correlation between structural features and catalytic activities of the composite. Moderate substitution and well-dispersion of iron in bimetallic sulfide composites are believed to have positive effect on the adsorption and activation of oxygen-containing species, thus leading to conspicuous ORR and OER catalytic enhancement compared to their monometallic counterparts. Besides, the covalent bridge between active sulfide particles and mesoporous carbon shells provides facile pathways for electron and mass transport. Beneficially, the intimate coupling interaction renders prolonged electrocatalytic performances to the composite. Our results may possibly lend a new impetus to the rational design of bi- or multimetallic sulfides encapsulated in porous carbon with improved performance for electrocatalysis and energy storage applications.

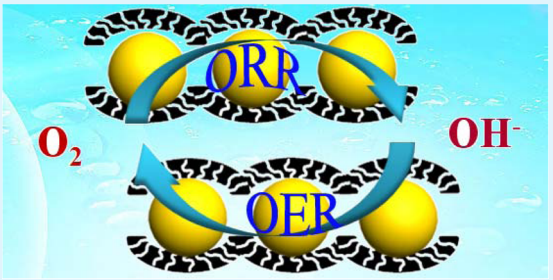

KEYWORDS: *fuel cells, electrocatalysts, late transition metal chalcogenides, mesoporous carbon, oxygen reduction reaction, oxygen evolution reaction*

1. INTRODUCTION

With the increasing concerns about the imminent global energy crisis, numerous efforts have been made to develop renewable and clean energy conversion and storage technologies for next-generation devices.[1,2] The effective conversion associated with chemical energy and electric energy can be realized with devices such as fuel cells, metal–air batteries, and electrolysis cells. However, their commercialization hurdles mainly lie in the intrinsically high kinetic barriers for ORR (oxygen reduction reaction) and OER (oxygen evolution reaction), which both proceed via four-electron pathways.[3−8] Hitherto, Pt and a few other precious metals, such as Ru- and Ir-based compounds, are highly active and widely applied catalysts for oxygen electrochemistry. Nonetheless, considering the limited availability and declining stability of precious-metal catalysts, the desire for industrial processes that incorporate earth-abundant nonprecious materials negotiating ORR and OER is intensifying the search for these materials.[9−11]

Over the past decades, nonprecious late transition metal chalcogenides (LTMCs) consisting of metal atoms such as Fe, Co, Ni, and chalcogen atoms such as S, Se, and Te have aroused enormous attention owing to their wide potential applications in high-temperature superconductors,[12,13] photovoltaics,[14,15] energy storage,[16−18] and electrocatalysis.[19−22] Back in 1974, Baresel et al. initiated the investigation on nonprecious LTMCs as catalysts for ORR.[23] Compared to noble metal catalysts, nonprecious LTMCs have evoked considerable interest with the merits of low cost, robust tolerance to small organic molecules, and high chemical kinetic stability both in acidic and basic media.[24−26] Notwithstanding these differences, it must be pointed out that the catalytic activities of nonprecious LTMCs still underperform the noble metal benchmark.

Tough attempts have been made to ameliorate the performance of nonprecious LTMCs negotiating ORR. Campbell's group explored Co–Se-,[27] FeS_2-,[28] and CoS_2[29]-based thin

Received: October 13, 2014
Accepted: December 22, 2014
Published: December 22, 2014

ACS Publications © 2014 American Chemical Society

DOI: 10.1021/am507033x
ACS Appl. Mater. Interfaces 2015, 7, 1207−1218

Scheme 1. Synthesis Process for $Co_{0.5}Fe_{0.5}S$@N-MC Composite

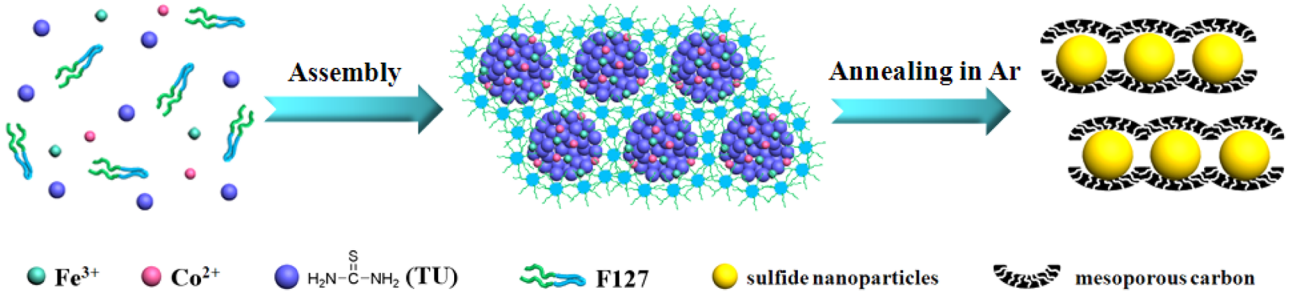

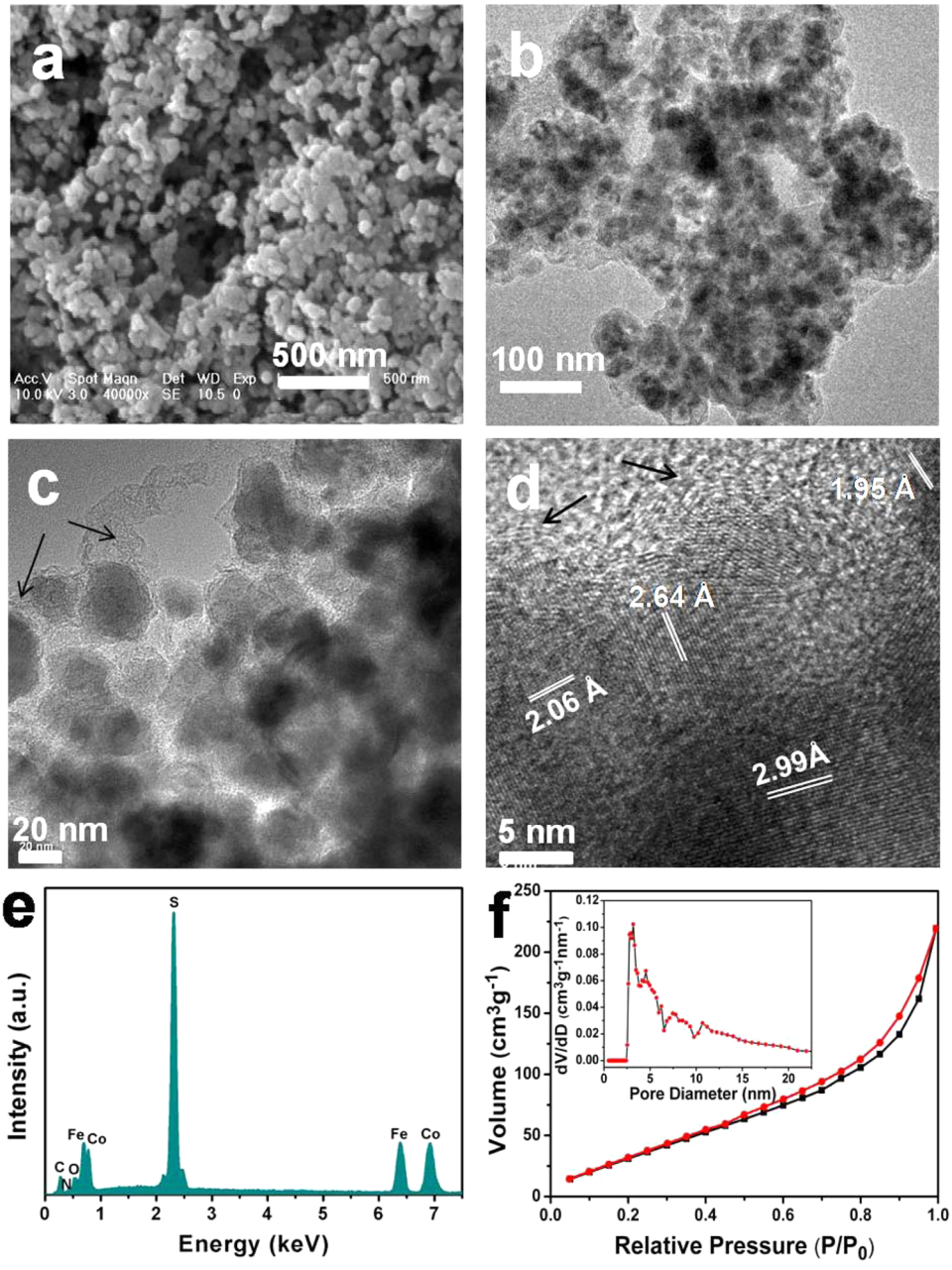

Figure 1. Typical (a) SEM, (b, c) TEM images, (d) high-resolution TEM image, (e) EDX analysis, and (f) N_2 adsorption−desorption isotherm of $Co_{0.5}Fe_{0.5}S$@N-MC composite annealed at 900 °C. (inset) The pore-size distribution curve.

films prepared by magnetron sputtering as appreciable catalysts for ORR in acidic medium. Magnetite Fe_3O_4 nanoparticles decorated $CoSe_2$-DETA nanobelts with a synergistically enhanced ORR activity compared with original $CoSe_2$-DETA was studied by Yu's group.[30] The conjunction with Fe_3O_4 was believed to create more active sites for O_2 absorption and

DOI: 10.1021/am507033x
ACS Appl. Mater. Interfaces 2015, 7, 1207−1218

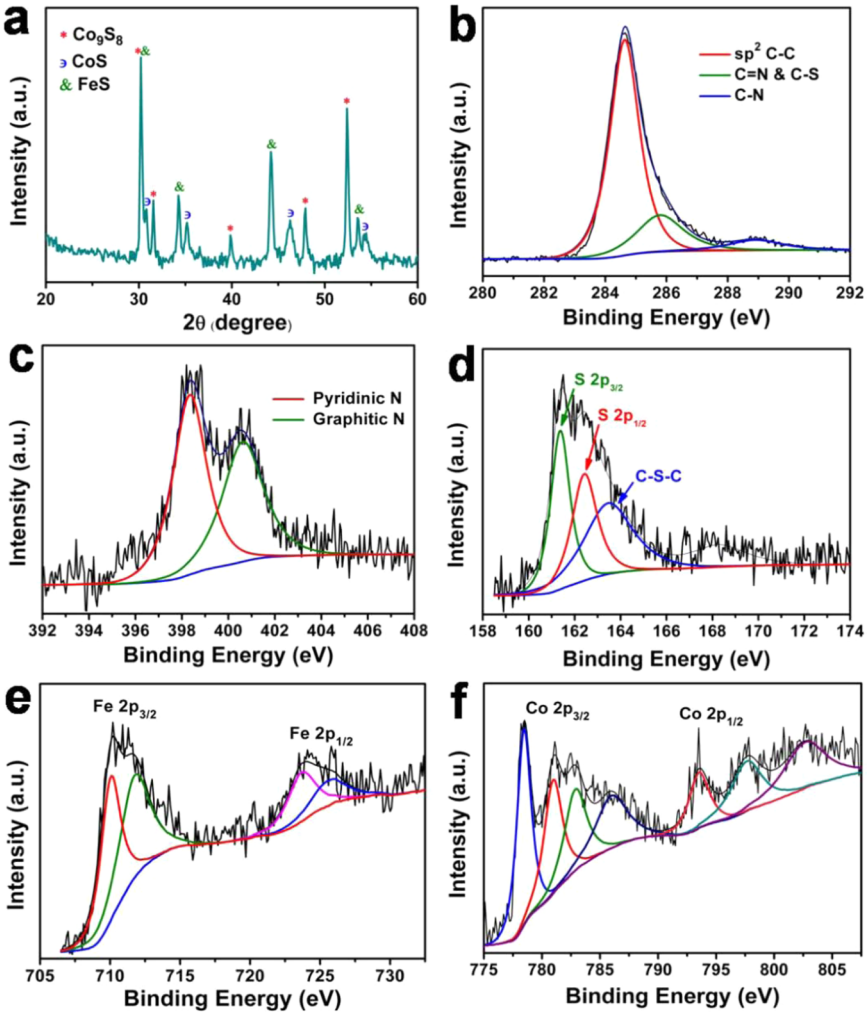

Figure 2. (a) XRD pattern and high-resolution (b) C 1s, (c) N 1s, (d) S 2p, (e) Fe 2p, and (f) Co 2p XPS spectra of $Co_{0.5}Fe_{0.5}S$@N-MC annealed at 900 °C.

activation. Yu's group also synthesized hierarchical hollow Co_9S_8 microspheres via a solvothermal reaction.[31] The ORR onset potential of Co_9S_8 microspheres was comparable to the predicted value from the theoretical simulation,[32] although its activity was still inferior to that of Pt/C. Recently Dai's group constructed strong coupling $Co_{1-x}S$/RGO hybrid material with excellent ORR catalytic performance.[33] The hybrid was endowed with desirable conductivity and reasonable stability mediated by the RGO template, and this made it a promising inexpensive cathode electrocatalyst for fuel cells. Although such headway has been made, there still are persistently high expectations for optimizing the catalytic behavior of nonprecious LTMCs with simple and low-cost synthetic routes. The challenges still remain to rationalize and design novel nonprecious LTMCs structures with certain characteristics to break through their dilemma for electrocatalysis.

Various investigations concluded the catalytic activity decreasing tendency as Co > Ni > Fe and S > Se > Te for nonprecious LTMCs.[24,34] And the highest catalytic activity of cobalt sulfide among nonprecious LTMCs was ascribed to the minimal energy gap between the oxygen 2p orbital and the highest occupied d-orbital of cobalt sulfide.[23,25] Here we report a facile soft-template mediated approach for fabrication of nanostructured cobalt−iron double sulfides that are covalently entrapped in nitrogen-doped mesoporous graphitic carbon ($Co_{0.5}Fe_{0.5}S$@N-MC). It turns out that incorporation of FeS in the composite is related to the favorable formation of cubic phase Co_9S_8, a higher active center for ORR. Besides, moderate substitution and well-dispersion of iron in bimetallic sulfides composite lead to favorable adsorption of oxygen-containing species and catalytic enhancement compared to their monometallic counterparts. At the same time, covalently assembling with mesoporous graphitic carbon is believed to facilitate charge transport and mass diffusion during catalysis. Fascinatingly, the bimetallic sulfides composite with modified nominal composition not only attains breakthroughs catalyzing ORR among the nonprecious LTMCs but catalyzes OER effectively in alkaline medium.

2. RESULTS AND DISCUSSION

2.1. Synthesis and Characterization. The simple and scalable synthesis procedure is illustrated in Scheme 1. An inexpensive and easily available industrial product, thiourea (TU), is adopted as the carbon and sulfur source, whereas a triblock polymeric surfactant (Pluronic F127) acts as the soft template precursor. During the evaporation-induced self-assembly process, TU, with the abundant functional groups C═S and $-NH_2$ tends to trap the cobalt and iron ions (with a Fe/Co molar ratio of 1:1). The hydrogen bond interaction between TU and amphiphilic F127 promotes the assembly

DOI: 10.1021/am507033x
ACS Appl. Mater. Interfaces 2015, 7, 1207−1218

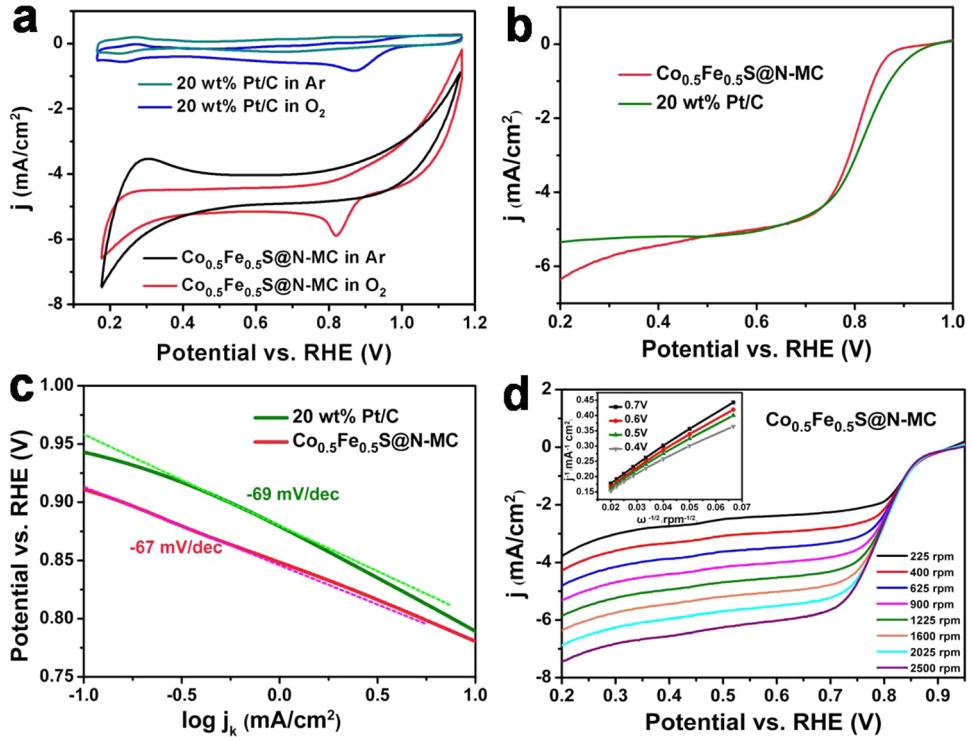

Figure 3. (a) CV curves in Ar- and O_2-saturated 0.1 M KOH. (b) Polarization curves at 1600 rpm in O_2-saturated 0.1 M KOH. (c) The mass transport-corrected Tafel plots derived from the corresponding RDE data of $Co_{0.5}Fe_{0.5}S$@N-MC and 20 wt % Pt/C. (d) Polarization curves of $Co_{0.5}Fe_{0.5}S$@N-MC at different rotating speeds. (inset) The corresponding Koutecky–Levich plots at different potentials derived from RDE.

process. Finally, after annealing the assembled composite in Ar atmosphere at 900 °C, cobalt–iron sulfide nanoparticles embedded in mesoporous graphitic carbon framework are generated. In fact, a variety of key factors may contribute to the successful synthetic process: (i) excess thiourea is intended for the simultaneous deposition of metallic sulfides and the formation of N-doped graphitic carbon matrix, thus averting unnecessary introduction of foreign carbon sources by tedious impregnation; (ii) complex crystalline structures of cobalt–iron double sulfides are spontaneously entrapped inside the graphitic carbon nanoshells, and at the same time undesirable oxidation is avoided during the annealing process protected by the inert atmosphere; (iii) with the removal of triblock F127 in pyrolysis, the carbon layer exhibits an accessible mesoporous feature, thus facilitating the electrolyte infiltration and mass transfer during catalysis.

Typical scanning electron microscopy (SEM) and transmission electron microscopy (TEM) investigations were carried out to provide insights into the morphologies and microstructures of the composite. SEM image revealed that nanostructured cobalt–iron bimetallic sulfide particles were relatively uniform and well-dispersed (Figure 1a). TEM images confirmed that sulfide nanocrystals with diameters of 20–40 nm were densely anchored inside the folded carbon film fragments with low aggregation (Figure 1b,c). The heat-treatment formation of well-defined graphitic carbon shell structure (black arrow in high-resolution (HR) TEM, Figure 1d) with the measured lattice spacing ranging from ~0.34 to 0.36 nm may favor the in situ incorporation of nitrogen,[35] thereby optimizing the electroconductivity of the composite.[36] More importantly, aggregation of sulfide nanoparticles was efficiently alleviated due to the tight wrapping of carbon shell.

Energy-dispersive X-ray spectroscopy (EDX) analysis (Figure 1e) disclosed the existence of C, N, S, Fe, Co, and O elements in the composite. The accurate atomic ratio of Co to Fe was ~1.0, which was in accordance with the molar ratios of their precursors. By calculation, the atomic ratio of S to the overall M (M = Fe, Co) was nearly 1.0 (see Table S1 in the Supporting Information), indicating the formation of $Co_{0.5}Fe_{0.5}S$. The atomic contents of C and N were 41.65 and 6.89 atom % respectively, which revealed simultaneous incorporation of a high level of nitrogen into the graphitic lattice. In addition, the composite had a relatively large Brunauer–Emmett–Teller (BET) specific surface area of 125 $m^2\ g^{-1}$ determined by the N_2 sorption measurement (Figure 1f), which was remarkably higher than that synthesized without F127 (17.4 $m^2\ g^{-1}$). The pore-size distribution curve evidenced that the composite possessed mesopores (3–8 nm) primarily deriving from the block copolymer.[37,38] The unique mesoporous channels of the carbon wall could undoubtedly provide facile pathways for mass transport to its internal reactive sites, thus facilitating the catalytic performance.[39] Correspondingly, the composite was designated as $Co_{0.5}Fe_{0.5}S$@N-MC with its nominal composition. According to thermogravimertic analysis (TGA) measurements in air (Supporting Information Figure S1), the mass fraction of bimetallic sulfides in the composite was ~72 wt %. Note that the major weight loss between 400 and 800 °C in the TGA curve corresponded to the removal of mesoporous carbon, while the slight weight decrease above 800 °C was due to the oxidation of sulfides in air.

The crystal structure of cobalt–iron double sulfides composite was investigated by the powder X-ray diffraction (XRD) technique. As shown in Figure 2a, three different groups of diffraction peaks could be indexed to well-crystallized hexagonal FeS (JCPDS card No. 65–9124), cubic Co_9S_8

DOI: 10.1021/am507033x
ACS Appl. Mater. Interfaces 2015, 7, 1207–1218

(JCPDS card No. 65−6801), and hexagonal CoS (JCPDS card No. 65−3418), respectively, indicating the formation of complicated and well-mixed bimetallic sulfides. The HRTEM image in Figure 1d confirmed that the lattice interplanar spacings of ∼2.64 and 2.06 Å corresponded to the distances of (101) and (102) planes of hexagonal FeS, respectively. The lattice fringes with spacings of 2.99 and 1.95 Å were also detected in the HRTEM image region, which matched well with the (311) plane of cubic Co_9S_8 and (102) plane of hexagonal CoS, respectively. The inherent complex stoichiometric of cobalt chalcogenides led to the generation of mixed Co_9S_8 and CoS phases. According to the Rietveled refinement results, the mass fractions of Co_9S_8 and CoS in cobalt sulfide phases were 64% and 36%, respectively. Sidik and Anderson proved that Co_9S_8 was a highly active site toward O_2 reduction.[32] We believed that the reasonable existence of mixed cobalt sulfide phases and pure FeS may create more reactive sites favorable for electrocatalysis.

X-ray photoelectron spectroscopy (XPS) analysis was performed to investigate the surface electron states properties of the elements. Bonding configurations of C, N, S, Fe, and Co for the composite were precisely shown in HR XPS spectra (Figure 2b−f). The prominent C 1s peak centered at 284.6 eV suggested the formation of sp^2 graphitic structure. C 1s peak at about 285.8 eV arose from C═N and C−S,[40,41] while the peak at ∼288.8 eV was assigned to C−N. The in situ generation of sp^2-hybridized graphitic carbon framework implied the improvement of electroconductivity, which favored fast electron transfer throughout the structural framework. The binding energy peaks observed in the HR N 1s profile at 398.3 and 400.6 eV were attributed to pyridinic and graphitic N, respectively. It was previously proven that pyridinic N could improve the onset potential, while graphitic N determined the limiting current for ORR.[42] In S 2p spectrum, the first two peaks located at 161.4 and 162.5 eV were due to the spin−orbit coupling in metal sulfide,[16,19] while S 2p peak at 163.5 eV suggested the covalent binding of S to C for $Co_{0.5}Fe_{0.5}S$@N-MC,[40,43] indicating that cobalt−iron double sulfide nanoparticles were covalently assembled in nitrogen-doped mesoporous graphitic carbon. The spectrum of Fe 2p was finely fitted with two spin−orbit doublets arising from $2p_{3/2}$ and $2p_{1/2}$ signals. The $2p_{3/2}$ peak of Fe at 710.1 and 711.9 eV corresponded to +2 oxidation state of Fe in FeS.[44] As to Co 2p spectrum, the first doublet at 778.4 and 793.5 eV indicated the dominance of Co^{2+} oxidation state with a mixed composition of Co_9S_8 and CoS, which was in good agreement with the results in the literature.[18,45,46]

2.2. Catalytic Studies. As mentioned above, the intentionally fabricated cobalt−iron double sulfide composite exhibited certain characteristics conducive to electrocatalysis. The ORR electrocatalytic behavior of $Co_{0.5}Fe_{0.5}S$@N-MC was first examined by cyclic voltammetry in Ar- and O_2-saturated 0.1 M KOH. As shown in Figure 3a, no obvious cathodic peak was observed in the absence of O_2 in the CV curve. Impressively, an appreciable cathodic peak located at 0.82 V appeared in oxygen-saturated solution for $Co_{0.5}Fe_{0.5}S$@N-MC. Noticeably, the composite showed a higher peak current (1.39 mA cm^{-2}) than that of Pt/C (0.833 mA cm^{-2}), clearly suggesting the pronounced ORR catalytic activity for $Co_{0.5}Fe_{0.5}S$@N-MC.

Rotating disk electrode (RDE) measurement was employed to gain further insight into the ORR kinetics. As shown in the polarization curves (Figure 3b), $Co_{0.5}Fe_{0.5}S$@N-MC exhibited an onset potential at 0.913 V (vs RHE) and reached a current density of 5.0 mA cm^{-2} at 0.60 V. The half-wave potential ($E_{1/2}$) of the composite was ∼0.808 V, which was only ∼5 mV deviation from Pt/C. With a steeper slope in the kinetic region and a higher diffusion-limiting current density at negative potentials, $Co_{0.5}Fe_{0.5}S$@N-MC displayed substantially superb activity comparable to Pt/C. Although its activity was still inferior to Pt/C benchmark at the same mass loading (Supporting Information, Figure S2), the low-cost and facile fabrication was a substantial advantage. The superb catalytic behavior was also reasonably retained at low mass loading of 0.1 mg/cm^2 (Supporting Information Figure S3). Moreover, the mass-transport corrected Tafel plots in the low current density regions were acquired based on the corresponding RDE data. As seen in Figure 3c, $Co_{0.5}Fe_{0.5}S$@N-MC displayed a smaller Tafel slope (67 mV/decade) than Pt/C (69 mV/decade), revealing its high kinetic specific activity. To the best of our knowledge, the exceptional catalytic performance of $Co_{0.5}Fe_{0.5}S$@N-MC made it a record-breaking one among the previously reported nonprecious LTMCs catalysts for ORR in alkaline medium, and the detailed comparison was demonstrated in Supporting Information (Table S2).

To reveal the electron transfer mechanism of the composite, Koutecky−Levich (K-L) plots derived from RDE measurements were employed (Figure 3d). The good linearity and near parallelism properties of K-L plots suggested first-order reaction kinetics toward the concentration of dissolved O_2 and similar electron transfer numbers for ORR at different potentials. According to the K-L equation, the electron transfer number (n) of $Co_{0.5}Fe_{0.5}S$@N-MC was calculated to be 3.8−4.0, indicating that the ORR from 0.4 to 0.7 V was ideal quasi-four-electron pathway of converting oxygen to OH^-. Additionally, rotating ring-disk electrode (RRDE) measurements at 1600 rpm were carried out to quantify the amount of the ORR intermediate, peroxide (H_2O_2). On the basis of eqs 5 and 6, the average peroxide yield was ∼6%, giving n above 3.7 throughout the investigated potential range (Supporting Information, Figure S4). The result further implied that the composite favored a dominating four-electron reduction of O_2 to OH^-, similar to ORR catalyzed by the commercial Pt/C. A dominative selectivity of four-electron reduction suggested a better ORR electrocatalytic efficiency for the composite.

Indeed, structural features of the composite, including atomic ratios of cobalt to iron in bimetallic sulfides and the loading levels of sulfides in mesoporous carbon combined with sulfide crystallinity affected by annealing temperature, were believed to exert significant contributions to the total catalytic activity. Therefore, structures of the composite were readily tuned to elucidate their correlation with the activities. First, varied iron substitution (x) in $Co_{1-x}Fe_xS$@N-MC (x = 0, 0.25, 0.50, 0.75, 1.0) was obtained by simply adjusting the initial molar ratios of cobalt and iron precursors. Supporting Information, Table S1 summarized the overall elemental values of as-prepared $Co_{1-x}Fe_xS$@N-MC composites from the detection of EDX, in which the stoichiometric ratios of cobalt to iron were very close to the molar ratios of their precursors during the synthesis. The morphologies of $Co_{1-x}Fe_xS$@N-MC (x = 0, 0.25, 0.75, 1.0) were also characterized with TEM (Supporting Information Figure S5), which revealed quite different microstructures and particle sizes of cobalt sulfide and iron sulfide in mono- and bimetallic composites. Although monometallic FeS@N-MC delivered sluggish ORR activity due to the intrinsic low activity of FeS,[24] moderate iron incorporation in the composite took positive effect on the improvement of the catalytic behavior.

DOI: 10.1021/am507033x
ACS Appl. Mater. Interfaces 2015, 7, 1207−1218

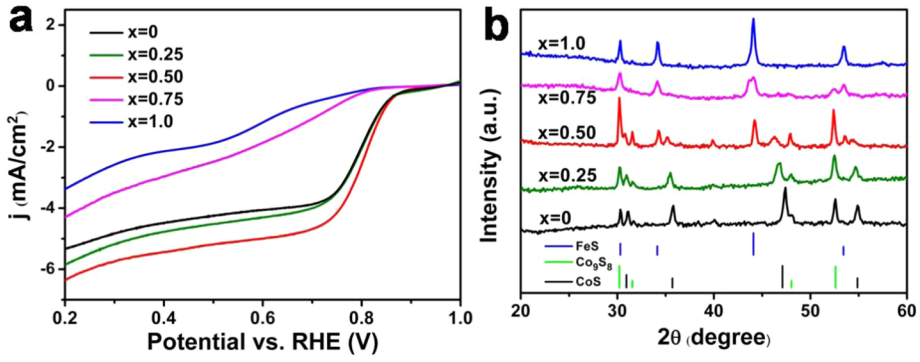

Figure 4. (a) Polarization curves of $Co_{1-x}Fe_xS$@N-MC (x = 0, 0.25, 0.50, 0.75, 1.0) at 1600 rpm in O_2-saturated 0.1 M KOH. (b) XRD patterns of $Co_{1-x}Fe_xS$@N-MC (x = 0, 0.25, 0.50, 0.75, 1.0).

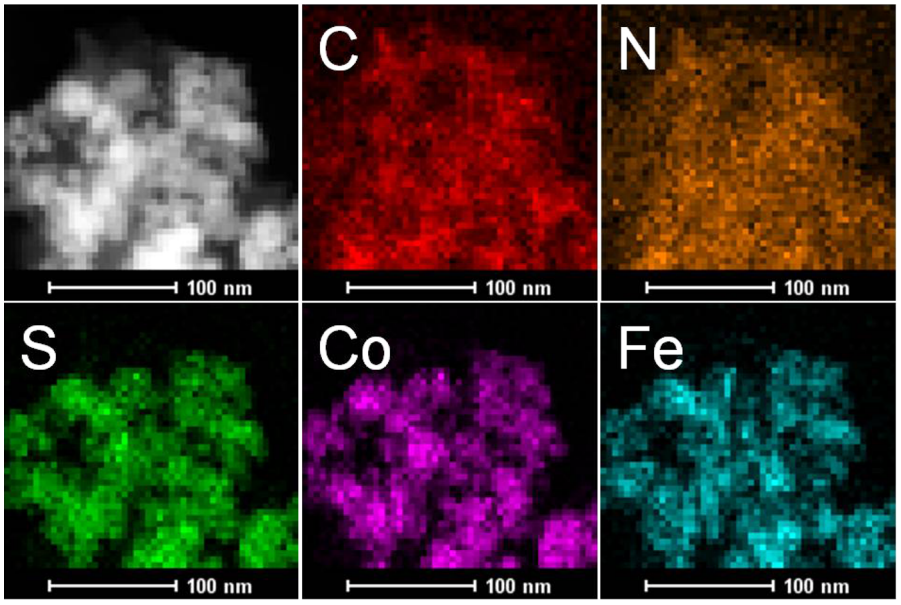

Figure 5. EELS elemental mapping analysis of $Co_{0.5}Fe_{0.5}S$@N-MC.

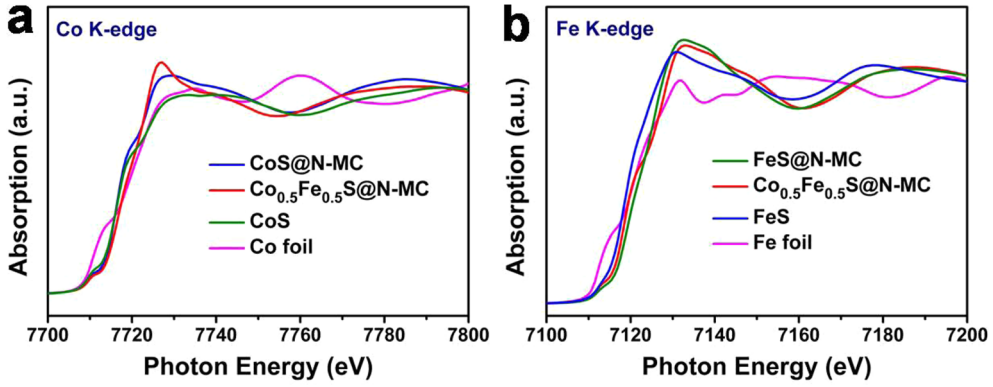

Figure 6. Normalized X-ray absorption near edge structure spectra at (a) Co K-edge and (b) Fe K-edge of $Co_{1-x}Fe_xS$@N-MC (x = 0, 0.5, 1.0) with CoS, Co foil, FeS, and Fe foil for references.

Among the composite with varied iron substitution, $Co_{0.5}Fe_{0.5}S$@N-MC displayed substantially the highest activity with the steepest slope in the kinetic region and earliest reach to the diffusion-limiting current density (Figure 4a). The activity enhancement was also observed in the physical mixture of CoS@N-MC and FeS@N-MC (Supporting Information, Figure S6), evidencing the positive synergy effect in the bimetallic composites.

The Rietveled refinement results based on XRD patterns ascertained that the fraction of cubic Co_9S_8 in cobalt sulfide phases was only 40% for CoS@N-MC, and this value increased to 100% for $Co_{0.25}Fe_{0.75}S$@N-MC (Figure 4b and Supporting Information, Table S3). It was thus inferred that with increase

DOI: 10.1021/am507033x
ACS Appl. Mater. Interfaces 2015, 7, 1207−1218

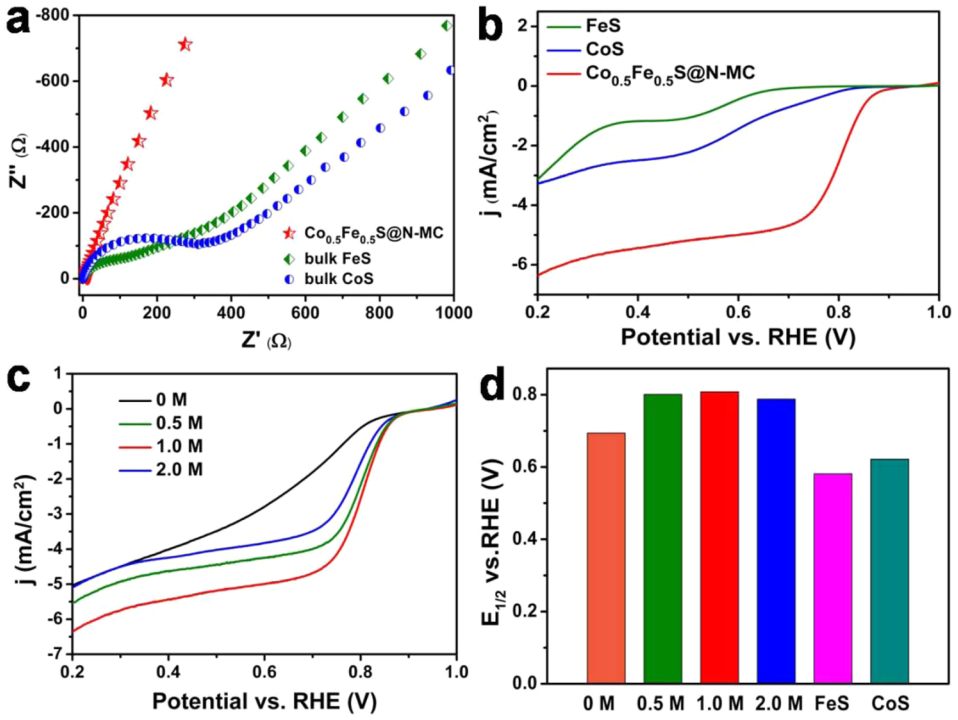

Figure 7. (a) Nyquist plots of electrochemical impedance data. (b) Polarization curves at 1600 rpm in O_2-saturated 0.1 M KOH for $Co_{0.5}Fe_{0.5}S$@N-MC and bulk FeS, CoS. (c) Polarization curves, and (d) the half-wave potentials ($E_{1/2}$) for $Co_{0.5}Fe_{0.5}S$@N-MC composite with different sulfide loading amounts at 1600 rpm in O_2-saturated 0.1 M KOH.

of iron substitution in the composite, cubic Co_9S_8 instead of hexagonal CoS was dominantly generated maybe due to the competitive hexagonal FeS product. Additionally, electron energy-loss spectroscopy (EELS) elemental mapping provided further evidence of the composition and structure of $Co_{0.5}Fe_{0.5}S$@N-MC (Figure 5), in which both the carbon and nitrogen species were evenly distributed throughout the nanostructure, while sulfur, cobalt, and iron signals were homogeneously overlaid in the nanoparticles with no obvious phase segregation. We speculated that since cobalt sulfide and iron sulfide had similar crystal structures, they tended to generate ternary cobalt−iron sulfides in the composite. Theoretical calculations based on d-band center model evidenced that Fe atom gave lower oxygen adsorption barriers than Co atom.[1,47] It was expected that moderate incorporation and thorough dispersion of iron sulfide would be highly beneficial for the adsorption and activation of oxygen,[28] thus leading to modified ORR performance for $Co_{0.5}Fe_{0.5}S$@N-MC composite. On the other hand, excess existence of FeS in $Co_{0.25}Fe_{0.75}S$@N-MC may shelter a large part of ORR-active cobalt sulfides surface. Therefore, large exposure of cobalt sulfides and moderate iron sulfide incorporation accounted for the synergistic enhanced catalytic behavior in $Co_{0.5}Fe_{0.5}S$@N-MC.

X-ray absorption spectroscopy (XAS) technique was a precise and element-specific experimental probe widely applied in studying catalyst materials to gain better understandings of their atomic structure, chemical state, and bonding characteristics.[48−52] There is spectral agreement and similar half-height edge positions between CoS@N-MC, $Co_{0.5}Fe_{0.5}S$@N-MC and CoS in normalized X-ray absorption near edge structure (XANES) spectra at Co K-edge (Figure 6a), declaring the similar electron state of Co.[53,54] However, an evident absorption intensity increase in CoS@N-MC and $Co_{0.5}Fe_{0.5}S$@N-MC spectra was determined compared to CoS. The conspicuous intensity change in the white line was probably affected by different electronic structures and surroundings of Co. This evidence suggested that sulfides were covalently bonding to carbon in the composite,[55,56] which was consistent with the results in C and S XPS spectra. Furthermore, the dominative cubic phase Co_9S_8 (occupying 64%) instead of hexagonal phase CoS in $Co_{0.5}Fe_{0.5}S$@N-MC probably accounted for the highest peak intensity at Co K-edge spectra. In terms of Fe K-edge XANES spectra (Figure 6b), the spectra consensus between FeS@N-MC, $Co_{0.5}Fe_{0.5}S$@N-MC, and FeS verified the dominating ferrous valence, consistent with the XPS result. Moreover, it was also inferred that the peak intensity increases were due to the electron coupling effect with carbon.

Notably, the covalent interaction between sulfides and graphitic carbon was worth highlighting, for remarkable improvement of electroconductivity was reasonably achieved for the composite. Nyquist plots based on electrochemical impedance spectroscopy (EIS) analysis exhibited a much smaller semicircle as well as a lower real axis intercept in the high-frequency region for $Co_{0.5}Fe_{0.5}S$@N-MC (Figure 7a), manifesting its superior electroconductivity to bulk CoS, FeS. The unique structural modification and synergistic effect in $Co_{0.5}Fe_{0.5}S$@N-MC undoubtedly facilitated the charge transport and elevated its ORR catalytic activity compared to commercial bulk CoS and FeS (Figure 7b and Supporting Information, Figure S7). Additionally, catalytic activity was also studied as a function of the sulfide loading mass content. The sulfide loading levels were controlled to be 0, 46, 72, and 90 wt % by adjusting the initial total molar weight of cobalt and iron precursors from 0 to 48 mmol (denoted as 0, 0.5, 1.0, and 2.0 M). Typical TEM images (Supporting Information, Figure S8) uncovered the morphologies of $Co_{0.5}Fe_{0.5}S$@N-MC (0, 0.5, 1.0,

DOI: 10.1021/am507033x
ACS Appl. Mater. Interfaces 2015, 7, 1207−1218

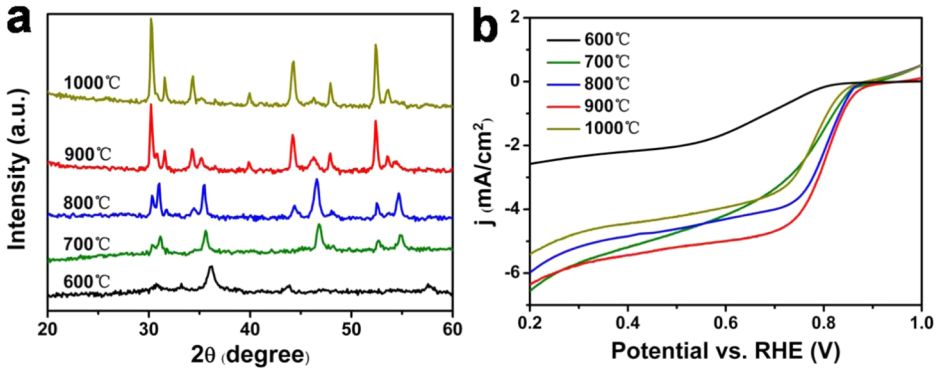

Figure 8. (a) XRD patterns of $Co_{0.5}Fe_{0.5}S$@N-MC obtained at different annealing temperatures. (b) Polarization curves of $Co_{0.5}Fe_{0.5}S$@N-MC obtained at different annealing temperatures in O_2-saturated 0.1 M KOH (1600 rpm).

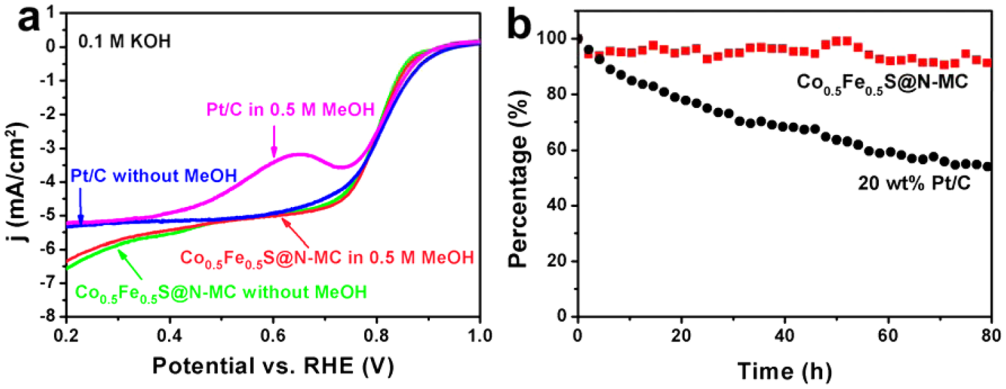

Figure 9. (a) Polarization plots of $Co_{0.5}Fe_{0.5}S$@N-MC and 20 wt % Pt/C in O_2-saturated 0.1 M KOH without and with addition of 0.5 M methanol. (b) Chronoamperometry (i–t) measurements of $Co_{0.5}Fe_{0.5}S$@N-MC and 20 wt % Pt/C in O_2-saturated 0.1 M KOH at 0.6 V (vs RHE), 225 rpm.

2.0 M). N and S dual-doped mesoporous carbon (N/S-MC) was obtained without addition of metal salts, and it was featured with wrinkled and folded film fragments (Supporting Information, Figure S8a). Bimetallic sulfide particles with diameters less than 20 nm were anchored inside the mesoporous carbon for $Co_{0.5}Fe_{0.5}S$@N-MC (0.5 M, Supporting Information, Figure S8b), and the particles were relatively fewer than $Co_{0.5}Fe_{0.5}S$@N-MC (1.0 M, Supporting Information, Figure S8c). With increased sulfide loading to generate $Co_{0.5}Fe_{0.5}S$@N-MC (2.0 M, Supporting Information, Figure S8d), the particles were prone to aggregation with diameters larger than 100 nm. The broad diffraction peaks of N/S-MC centered at approximately 25.2° and 43.2° were characteristic (002) and (100) reflections of graphitic carbon (Supporting Information, Figure S9a). With the increase of sulfide loading amount, planes of the graphitic carbon disappeared, and the characteristic peak intensities of FeS, Co_9S_8, and CoS increased gradually. On the other hand, the weight fraction of S was 6.24 wt % in N/S-MC and increased to 34.39 wt % in $Co_{0.5}Fe_{0.5}S$@N-MC (2.0 M) due to its coprecipitation with cobalt and iron (Supporting Information, Table S4). The mass fraction increase of bimetallic sulfides was accompanied by the abundance of active sites, whereas the particle agglomeration and deterioration of conductivity were inevitable at high sulfide loading (Supporting Information, Figures S8d and S9b). Hence, $Co_{0.5}Fe_{0.5}S$@N-MC with 72 wt % $Co_{0.5}Fe_{0.5}S$ (denoted as 1.0 M) displayed the highest activity for ORR with the most positive half-wave potential ($E_{1/2}$) (Figure 7c,d).

More importantly, annealing temperature also played a vital role in optimizing the structural features of the $Co_{0.5}Fe_{0.5}S$@N-MC composite. It can be seen from XRD patterns that few cobalt–iron double sulfides were generated below 800 °C, and higher annealing temperature was in favor of formation of well-crystallized cobalt–iron bimetallic sulfides (Figure 8a). However, the gasification of carbon at 1000 °C resulted in serious decrease of BET specific surface area to 79 $m^2\ g^{-1}$. Thus, an optimal balance of sulfide crystallinity and porous feature may account for the maximum ORR activity for $Co_{0.5}Fe_{0.5}S$@N-MC at 900 °C (Figure 8b). In fact, a strong correlation between the activity and mesoporous structures of the composite was observed. As can be seen in the polarization curves and CV curves (Supporting Information Figure S10), the composite synthesized without Pluronic F127 delivered apparently poorer ORR activity mainly due to its low specific surface area (17.4 $m^2\ g^{-1}$). Relatively high BET specific surface area (124.5 $m^2\ g^{-1}$) and pore volume (0.339 $cm^3\ g^{-1}$) of $Co_{0.5}Fe_{0.5}S$@N-MC at 900 °C undoubtedly provided facile mesoporous pathways for the diffusion of oxygen and the electrolyte, which exerted significant contributions to its superb catalytic activity.

For the practical applications of methanol fuel cell systems, robust tolerance to methanol crossover, combined with long-term chemical kinetic stability, were critical criterions for cathode electrocatalysts. As demonstrated in the polarization curve (Figure 9a), with addition of 0.5 M methanol, the catalytic activity of Pt/C deviated seriously due to its undesirable activity for methanol oxidation reaction (MOR) simultaneously occurring at the cathode. In contrast, nonprecious LTMCs catalysts were prevalently validated to circumvent the deactivation problem of methanol poisoning. The unaltered

DOI: 10.1021/am507033x
ACS Appl. Mater. Interfaces 2015, 7, 1207–1218

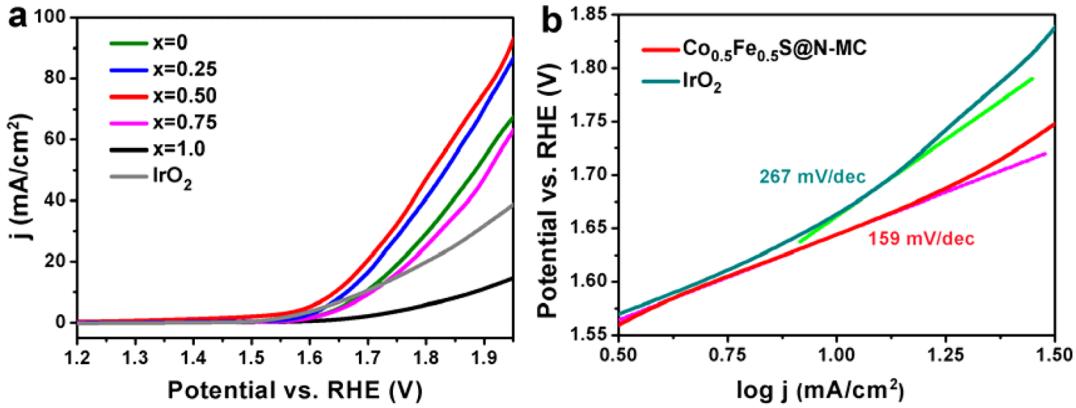

Figure 10. (a) Linear sweep voltammetry polarization curves of $Co_{1-x}Fe_xS$@N-MC (x = 0, 0.25, 0.50, 0.75, 1.0) and IrO_2 in 1 M KOH, Ar-saturated; scan rate: 5 mV s^{-1}. (b) OER Tafel plots derived from polarization curves for $Co_{0.5}Fe_{0.5}S$@N-MC and IrO_2.

catalytic behavior for $Co_{0.5}Fe_{0.5}S$@N-MC in Figure 9a indicated that its resistance toward possible methanol crossover poisoning was robust in comparison to that of Pt/C. Furthermore, the durability testing was conducted at a potential of 0.6 V (vs RHE). As shown in the current−time (i−t) curve (Figure 9b), 89% of the initial current density after 80 h can be maintained for $Co_{0.5}Fe_{0.5}S$@N-MC, which was significantly higher than that of Pt/C (54%). Additionally, $Co_{0.5}Fe_{0.5}S$@N-MC after ORR measurement retained similar edge structure characteristics to those of the pristine ones at Co K-edge and Fe K-edge (Supporting Information Figure S11), suggesting nearly no valence state change happened after long-term electrochemical cycling. TEM characterization further demonstrated the morphology change of the composite after ORR test (Supporting Information Figure S12). It was postulated that the tight covalent attachment of sulfide nanoparticles into carbon shell imparted them with high catalytic stability.

Oxygen evolution reaction (OER), the rate-limiting step involved in electrochemical systems such as metal-air batteries and water splitting, holds a key to a wide range of renewable energy solutions.[57−59] Inspired by the extensive research on mixed late transition metal composite materials as electrocatalysts for OER,[19,21,60−63] we extended the operating potentials to the water oxidation regime for our materials afterward. The OER catalytic activity of $Co_{1-x}Fe_xS$@N-MC was assessed in Ar-saturated 1 M KOH in an anodic direction together with IrO_2 for comparison (Figure 10a). Among various iron substitutions in sulfide composites, $Co_{0.5}Fe_{0.5}S$@N-MC exhibited the earliest onset potential (~1.57 V) and manifested a current density of 10 mA cm^{-2} at the overpotential as low as 0.41 V, indicative of the lowest-energy input for driving OER. Note that FeS@N-MC alone had little catalytic activity for OER, whereas in the $Co_{0.5}Fe_{0.5}S$@N-MC composite, FeS acted as foreign synergist conducive to favorable adsorption and activation of H_2O molecules.[1,21,64]

The mass loading density of cobalt−iron bimetallic sulfides in mesoporous carbon also affected OER activity significantly. As shown in Supporting Information, Figure S13a, $Co_{0.5}Fe_{0.5}S$@N-MC with 72 wt % sulfide loading in mesoporous carbon (denoted as 1.0 M) afforded the most favorable OER activity, which coincided with its best ORR performance. The superb electroconductivity and large exposure of reactive sulfide surface were essential factors optimizing OER activity. On the basis of polarization curves, Tafel plots were obtained to investigate the OER kinetics in the low overpotential region (Figure 10b). A much lower slope (159 mV/decade) of $Co_{0.5}Fe_{0.5}S$@N-MC indicated a higher OER activity compared to IrO_2 (267 mV/decade). Chronopotentiometry (v−t) measurements were carried out at a constant anodic current density of 10 mA cm^{-2} for OER (Supporting Information Figure S13b). As recorded during the course of experiment, $Co_{0.5}Fe_{0.5}S$@N-MC showed only ~0.037 V overpotential increase after 20 000 s. The long-lasting viability, conferred upon it by strong coupling and synergistic electrochemical effect between sulfides and carbon shell, made it a potential nonprecious catalyst for OER.

3. CONCLUSIONS

In summary, nanostructured cobalt−iron double sulfides covalently encapsulated in nitrogen-doped mesoporous graphitic carbon with tunable nominal compositions were fabricated via an economically viable and scalable approach. The $Co_{0.5}Fe_{0.5}S$@N-MC composite not only demonstrated exceptionally prominent electrocatalytic activity and durability for ORR, but offered impressive catalytic performance for OER in alkaline medium. Various characterization techniques have offered us a reliable picture of structural information relative to the electroactive behavior. The outstanding ORR and OER performance of the composite was strongly correlated to the homogeneous distribution of cobalt−iron double sulfide active sites and synergetic coupling interaction with the well-defined mesoporous carbon shell. This earth-abundant and easily constructed composite could undoubtedly hold a great promise for other practical applications in energy conversion and storage techniques, such as lithium-ion batteries[16,17,65,66] and supercapacitors.[18,67,68]

4. EXPERIMENTAL SECTION

4.1. Preparation of $Co_{1-x}Fe_xS$@N-MC composites. Thiourea (CH_4N_2S, TU, 10 g) and amphiphilic triblock copolymers (Pluronic F127, $(EO)_{106}$-$(PO)_{70}$-$(EO)_{106}$, 2.5 g) were first dissolved in 50 mL of water at 80 °C. Cobalt(II) acetate and iron(III) nitrate aqueous solution (50 mL) with different molar ratios (x = 0, 0.25, 0.50, 0.75, 1.0) were added to the above mixture afterward. The total molar weights of iron and cobalt varied from 0 to 48 mmol for optimization, which were denoted as 0, 0.5, 1.0, and 2.0 M. The mixed solution was stirred vigorously to evaporate at 80 °C for ~20 h. After further heating at 110 °C for thermosetting, the dried homogeneous mixture was subsequently subjected to annealing under Ar

DOI: 10.1021/am507033x
ACS Appl. Mater. Interfaces 2015, 7, 1207−1218

atmosphere at different temperatures (600−1 000 °C) for 1 h with the heating rate of 5 °C min^{-1}. The obtained powder was then washed with ultrapure water and ethanol several times to remove the impurities. Finally, the samples were dried at 100 °C in an oven for 12 h to generate $Co_{1-x}Fe_xS$@N-MC composites.

4.2. Characterization. Scanning electron microscopy (SEM) images were recorded on a FEI/Philips XL30 ESEM FEG field-emission scanning electron microscope. Transmission electron microscopy (TEM) images were taken by a Hitachi H-8100 transmission electron microscope. HR TEM micrographs were obtained on a TECNAI G2 HR transmission electron microscope with an accelerating voltage of 200 kV. X-ray diffraction (XRD) characterization was carried out on a Bruker D8 Advance diffractometer (Germany) using Cu Kα (1.5406 Å) radiation. X-ray photoelectron spectroscopy (XPS) measurement was performed on a VG ESCALAB MKII spectrometer with Al Kα X-ray radiation as the X-ray source for excitation. Inductively coupled plasma optical emission spectrometry (ICP-OES) results were determined on an ELAN 9000/DRC system to analyze the content of Fe and Co. Elemental analysis was conducted on a Vario EL cube (Elementar Analysensysteme GmbH) to determine the content of carbon, nitrogen, and sulfur for the samples. The nitrogen adsorption/desorption data were measured at 77 K with a Quantachrome Adsorption Instrument. Thermogravimetric analysis (TGA) measurements were performed on a PerkinElmer TGA-2 thermogravimetric analyzer in air at a heating rate of 10 °C min^{-1} from 25 to 900 °C. X-ray absorption fine structure (XAFS) spectroscopy experiment was performed at 1W2B end station, Beijing Synchrotron Radiation Facility (BSRF). Fe and Co K-edge spectra were collected at room temperature in transmission mode. To gain optimal spectral data, the weighed powder samples were mixed with boron nitride homogeneously at appropriate mass ratios, followed by being pressed into tablets.

4.3. Electrochemical Measurements. All the electrochemical measurements were carried out on an electrochemical workstation in a standard three-electrode cell. Ag/AgCl and Pt wire were selected as the reference electrode and counter electrode, respectively. A glassy carbon (GC) rotating disk electrode (RDE) acted as the working electrode. The suspension of the catalyst ink with a concentration of 20 mg mL^{-1} was prepared by ultrasonically dispersing them (10 mg) in a mixture of ethanol (489 μL) and Nafion (11 μL, 5%). Then, 5.2 μL of the homogeneous mixture (1.3 μL for Pt/C) was loaded onto the surface of a prepolished glassy carbon electrode (GCE) followed by drying naturally in air, resulting in a catalyst loading of 0.8 mg cm^{-2} (0.2 mg cm^{-2} for Pt/C). ORR measurements were conducted in the electrolyte of 0.1 M KOH, which was saturated with oxygen during the experiments. The CV and polarization curves were run at a scanning rate of 10 mV s^{-1}. The rotation rates of RDE were set varying from 225 to 2 500 rpm to collect the polarization plot data. OER measurement was carried out in Ar-saturated 1 M KOH. The polarization curves were recorded at a scanning rate of 5 mV s^{-1}. Electrochemical impedance spectroscopy (EIS) analysis was performed on Solartron 1255B Frequency Response Analyzer (Solartron Inc., UK).

Potentials measured versus Ag/AgCl electrode were converted to a reversible hydrogen electrode (RHE) scale on the basis of Nernst equation as follows:

$$E_{RHE} = E_{Ag/AgCl} + 0.059(pH) + 0.197(V) \quad (1)$$

The number of electrons transferred (n) for ORR can be determined from the Koutecky−Levich (K-L) equation:[69]

$$\frac{1}{J} = \frac{1}{J_k} + \frac{1}{J_d} = \frac{1}{J_k} + \frac{1}{B\omega^{1/2}} \quad (2)$$

$$B = 0.2nFC_oD^{2/3}\mu^{-1/6} \quad (3)$$

in which J is the measured current density, F is the Faraday constant (F = 96 485 C mol^{-1}), C_o is the bulk concentration of O_2 in 0.1 M KOH ($C_o = 1.2 \times 10^{-6}$ mol cm^{-3}), D is the diffusion coefficient of O_2 ($D = 1.9 \times 10^{-5}$ cm^2 s^{-1}), μ is the kinematic viscosity of the electrolyte at room temperature (μ = 0.01 cm^2 s^{-1}), ω is angular velocity of the disk, J_k is the kinetic-limiting current density, and J_d is the diffusing-limiting current density. The constant 0.2 is adopted when the rotation rate is expressed in rpm.

J_k can be calculated from J_d according to eq 2:

$$J_k = \frac{J \times J_d}{J_d - J} \quad (4)$$

On the basis of the RRDE measurement, the H_2O_2 (%) and the electron transfer number (n) were calculated by eqs 5 and 6 as follows:

$$H_2O_2(\%) = 200 \times \frac{I_r/N}{I_d + I_r/N} \quad (5)$$

$$n = 4 \times \frac{I_d}{I_d + I_r/N} \quad (6)$$

where I_d is the disk current, I_r is the ring current, and N is the current collection efficiency.

■ ASSOCIATED CONTENT

Ⓢ Supporting Information

TGA spectra, polarization curves, TEM images, XRD patterns, Nyquist plots, Co and Fe K-edge XANES plots, tabulated summary of elemental values of composites as detected by EDX. This material is available free of charge via the Internet at http://pubs.acs.org.

■ AUTHOR INFORMATION

Corresponding Authors

*E-mail: klai@ciac.ac.cn. (K.A.)
*E-mail: lehuilu@ciac.ac.cn. (L.L.)

Notes

The authors declare no competing financial interest.

■ ACKNOWLEDGMENTS

We are grateful for the financial support by NSFC (No. 21125521). The staff members of Beijing Synchrotron Radiation Facility are greatly acknowledged for their support in experimental measurement and data processing.

■ REFERENCES

(1) Katsounaros, I.; Cherevko, S.; Zeradjanin, A. R.; Mayrhofer, K. J. J. Oxygen Electrochemistry as a Cornerstone for Sustainable Energy Conversion. *Angew. Chem., Int. Ed.* **2014**, *53*, 102−121.

(2) Yuan, C.; Wu, H. B.; Xie, Y.; Lou, X. W. Mixed Transition-Metal Oxides: Design, Synthesis, and Energy-Related Applications. *Angew. Chem., Int. Ed.* **2014**, *53*, 1488−1504.

DOI: 10.1021/am507033x
ACS Appl. Mater. Interfaces 2015, 7, 1207−1218

(3) Jahan, M.; Liu, Z.; Loh, K. P. A Graphene Oxide and Copper-Centered Metal Organic Framework Composite as a Tri-Functional Catalyst for HER, OER, and ORR. *Adv. Funct. Mater.* **2013**, *23*, 5363−5372.
(4) Li, Y.; Gong, M.; Liang, Y.; Feng, J.; Kim, J.-E.; Wang, H.; Hong, G.; Zhang, B.; Dai, H. Advanced Zinc-Air Batteries Based on High-Performance Hybrid Electrocatalysts. *Nat. Commun.* **2013**, *4*, 1805−1811.
(5) Suntivich, J.; May, K. J.; Gasteiger, H. A.; Goodenough, J. B.; Shao-Horn, Y. A Perovskite Oxide Optimized for Oxygen Evolution Catalysis from Molecular Orbital Principles. *Science* **2011**, *334*, 1383−1385.
(6) Zheng, Y.; Jiao, Y.; Ge, L.; Jaroniec, M.; Qiao, S. Z. Two-Step Boron and Nitrogen Doping in Graphene for Enhanced Synergistic Catalysis. *Angew. Chem., Int. Ed.* **2013**, *52*, 3110−3116.
(7) Duan, J.; Chen, S.; Dai, S.; Qiao, S. Z. Shape Control of Mn_3O_4 Nanoparticles on Nitrogen-Doped Graphene for Enhanced Oxygen Reduction Activity. *Adv. Funct. Mater.* **2014**, *24*, 2072−2078.
(8) Liang, J.; Zhou, R. F.; Chen, X. M.; Tang, Y. H.; Qiao, S. Z. Fe-N Decorated Hybrids of CNTs Grown on Hierarchically Porous Carbon for High-Performance Oxygen Reduction. *Adv. Mater.* **2014**, *26*, 6074−6079.
(9) Liang, Y.; Li, Y.; Wang, H.; Zhou, J.; Wang, J.; Regier, T.; Dai, H. Co_3O_4 Nanocrystals on Graphene as a Synergistic Catalyst for Oxygen Reduction Reaction. *Nat. Mater.* **2011**, *10*, 780−786.
(10) Gasteiger, H. A.; Kocha, S. S.; Sompalli, B.; Wagner, F. T. Activity Benchmarks and Requirements for Pt, Pt-alloy, and Non-Pt Oxygen Reduction Catalysts for PEMFCs. *Appl. Catal., B* **2005**, *56*, 9−35.
(11) Lefèvre, M.; Proietti, E.; Jaouen, F.; Dodelet, J.-P. Iron-Based Catalysts with Improved Oxygen Reduction Activity in Polymer Electrolyte Fuel Cells. *Science* **2009**, *324*, 71−74.
(12) Hanaguri, T.; Niitaka, S.; Kuroki, K.; Takagi, H. Unconventional s-Wave Superconductivity in Fe(Se,Te). *Science* **2010**, *328*, 474−476.
(13) Si, W.; Han, S. J.; Shi, X.; Ehrlich, S. N.; Jaroszynski, J.; Goyal, A.; Li, Q. High Current Superconductivity in $FeSe_{0.5}Te_{0.5}$-Coated Conductors at 30 T. *Nat. Commun.* **2013**, *4*, 1347−1351.
(14) Wang, M.; Anghel, A. M.; Marsan, B.; Cevey-Ha, N.-L.; Pootrakulchote, N.; Zakeeruddin, S. M.; Grätzel, M. CoS Supersedes Pt as Efficient Electrocatalyst for Triiodide Reduction in Dye-Sensitized Solar Cells. *J. Am. Chem. Soc.* **2009**, *131*, 15976−15977.
(15) Sun, H.; Qin, D.; Huang, S.; Guo, X.; Li, D.; Luo, Y.; Meng, Q. Dye-Sensitized Solar Cells with NiS Counter Electrodes Electrodeposited by a Potential Reversal Technique. *Energy Environ. Sci.* **2011**, *4*, 2630−2637.
(16) Wang, X.; Xiang, Q.; Liu, B.; Wang, L.; Luo, T.; Chen, D.; Shen, G. TiO_2 Modified FeS Nanostructures with Enhanced Electrochemical Performance for Lithium-Ion Batteries. *Sci. Rep.* **2013**, *3*, 2007−2014.
(17) Son, S.-B.; Yersak, T. A.; Piper, D. M.; Kim, S. C.; Kang, C. S.; Cho, J. S.; Suh, S.-S.; Kim, Y.-U.; Oh, K. H.; Lee, S.-H. *Adv. Energy Mater.* **2014**, DOI: 10.1002/aenm.201300961.
(18) Xu, J.; Wang, Q.; Wang, X.; Xiang, Q.; Liang, B.; Chen, D.; Shen, G. Flexible Asymmetric Supercapacitors Based upon Co_9S_8 Nanorod//Co_3O_4@RuO_2 Nanosheet Arrays on Carbon Cloth. *ACS Nano* **2013**, *7*, 5453−5462.
(19) Liu, Q.; Jin, J.; Zhang, J. $NiCo_2S_4$@graphene as a Bifunctional Electrocatalyst for Oxygen Reduction and Evolution Reactions. *ACS Appl. Mater. Interfaces* **2013**, *5*, 5002−5008.
(20) Feng, Y.; He, T.; Alonso-Vante, N. In situ Free-Surfactant Synthesis and ORR- Electrochemistry of Carbon-Supported Co_3S_4 and $CoSe_2$ Nanoparticles. *Chem. Mater.* **2008**, *20*, 26−28.
(21) Gao, M.-R.; Xu, Y.-F.; Jiang, J.; Zheng, Y.-R.; Yu, S.-H. Water Oxidation Electrocatalyzed by an Efficient Mn_3O_4/$CoSe_2$ Nanocomposite. *J. Am. Chem. Soc.* **2012**, *134*, 2930−2933.
(22) Kong, D.; Cha, J. J.; Wang, H.; Lee, H. R.; Cui, Y. First-Row Transition Metal Dichalcogenide Catalysts for Hydrogen Evolution Reaction. *Energy Environ. Sci.* **2013**, *6*, 3553−3558.
(23) Von Baresel, D.; Sarholz, W.; Scharner, P.; Schmitz, J. Übergangs-Metallchalkogenide als Sauerstoff-Katalysatoren für Brennstoffzellen. *Ber. Bunsen-Ges.* **1974**, *78*, 608−611.
(24) Feng, Y.; Gago, A.; Timperman, L.; Alonso-Vante, N. Chalcogenide Metal Centers for Oxygen Reduction Reaction: Activity and Tolerance. *Electrochim. Acta* **2011**, *56*, 1009−1022.
(25) Gao, M.-R.; Jiang, J.; Yu, S.-H. Solution-Based Synthesis and Design of Late Transition Metal Chalcogenide Materials for Oxygen Reduction Reaction (ORR). *Small* **2012**, *8*, 13−27.
(26) Gao, M.-R.; Xu, Y.-F.; Jiang, J.; Yu, S.-H. Nanostructured Metal Chalcogenides: Synthesis, Modification, and Applications in Energy Conversion and Storage Devices. *Chem. Soc. Rev.* **2013**, *42*, 2986−3017.
(27) Susac, D.; Sode, A.; Zhu, L.; Wong, P. C.; Teo, M.; Bizzotto, D.; Mitchell, K. A. R.; Parsons, R. R.; Campbell, S. A. A Methodology for Investigating New Nonprecious Metal Catalysts for PEM Fuel Cells. *J. Phys. Chem. B* **2006**, *110*, 10762−10770.
(28) Susac, D.; Zhu, L.; Teo, M.; Sode, A.; Wong, K. C.; Wong, P. C.; Parsons, R. R.; Bizzotto, D.; Mitchell, K. A. R.; Campbell, S. A. Characterization of FeS_2-Based Thin Films as Model Catalysts for the Oxygen Reduction Reaction. *J. Phys. Chem. C* **2007**, *111*, 18715−18723.
(29) Zhu, L.; Susac, D.; Teo, M.; Wong, K. C.; Wong, P. C.; Parsons, R. R.; Bizzotto, D.; Mitchell, K. A. R.; Campbell, S. A. Investigation of CoS_2-based Thin Films as Model Catalysts for the Oxygen Reduction Reaction. *J. Catal.* **2008**, *258*, 235−242.
(30) Gao, M.-R.; Liu, S.; Jiang, J.; Cui, C.-H.; Yao, W.-T.; Yu, S.-H. In situ Controllable Synthesis of Magnetite Nanocrystals/$CoSe_2$ Hybrid Nanobelts and Their Enhanced Catalytic Performance. *J. Mater. Chem.* **2010**, *20*, 9355−9361.
(31) Zhou, Y.-X.; Yao, H.-B.; Wang, Y.; Liu, H.-L.; Gao, M.-R.; Shen, P.-K.; Yu, S.-H. Hierarchical Hollow Co_9S_8 Microspheres: Solvothermal Synthesis, Magnetic, Electrochemical, and Electrocatalytic Properties. *Chem.—Eur. J.* **2010**, *16*, 12000−12007.
(32) Sidik, R. A.; Anderson, A. B. Co_9S_8 as a Catalyst for Electroreduction of O_2: Quantum Chemistry Predictions. *J. Phys. Chem. B* **2006**, *110*, 936−941.
(33) Wang, H.; Liang, Y.; Li, Y.; Dai, H. $Co_{1-x}S$-Graphene Hybrid: A High-Performance Metal Chalcogenide Electrocatalyst for Oxygen Reduction. *Angew. Chem., Int. Ed.* **2011**, *50*, 10969−10972.
(34) Behret, H.; Binder, H.; Sandstede, G. Electrocatalytic Oxygen Reduction with Thiospinels and Other Sulphides of Tansition Metals. *Electrochim. Acta* **1975**, *20*, 111−117.
(35) Wu, G.; More, K. L.; Johnston, C. M.; Zelenay, P. High-Performance Electrocatalysts for Oxygen Reduction Derived from Polyaniline, Iron, and Cobalt. *Science* **2011**, *332*, 443−447.
(36) Ai, K.; Liu, Y.; Ruan, C.; Lu, L.; Lu, G. Sp^2 C-Dominant N-Doped Carbon Sub-micrometer Spheres with a Tunable Size: A Versatile Platform for Highly Efficient Oxygen-Reduction Catalysts. *Adv. Mater.* **2013**, *25*, 998−1003.
(37) Wei, J.; Zhou, D.; Sun, Z.; Deng, Y.; Xia, Y.; Zhao, D. A Controllable Synthesis of Rich Nitrogen-Doped Ordered Mesoporous Carbon for CO_2 Capture and Supercapacitors. *Adv. Funct. Mater.* **2013**, *23*, 2322−2328.
(38) Chen, Y.; Song, B.; Li, M.; Lu, L.; Xue, J. Fe_3O_4 Nanoparticles Embedded in Uniform Mesoporous Carbon Spheres for Superior High-Rate Battery Applications. *Adv. Funct. Mater.* **2014**, *24*, 319−326.
(39) He, W.; Jiang, C.; Wang, J.; Lu, L. High-Rate Oxygen Electroreduction over Graphitic-N Species Exposed on 3D Hierarchically Porous Nitrogen-Doped Carbons. *Angew. Chem., Int. Ed.* **2014**, *53*, 9503−9507.
(40) Wohlgemuth, S.-A.; White, R. J.; Willinger, M.-G.; Titirici, M.-M.; Antonietti, M. A One-Pot Hydrothermal Synthesis of Sulfur and Nitrogen Doped Carbon Aerogels with Enhanced Electrocatalytic Activity in the Oxygen Reduction Reaction. *Green Chem.* **2012**, *14*, 1515−1523.
(41) Dong, Y.; Pang, H.; Yang, H. B.; Guo, C.; Shao, J.; Chi, Y.; Li, C. M.; Yu, T. Carbon-Based Dots Co-doped with Nitrogen and Sulfur for

DOI: 10.1021/am507033x
ACS Appl. Mater. Interfaces 2015, 7, 1207−1218

High Quantum Yield and Excitation-Independent Emission. *Angew. Chem., Int. Ed.* **2013**, *52*, 7800−7804.
(42) Lai, L.; Potts, J. R.; Zhan, D.; Wang, L.; Poh, C. K.; Tang, C.; Gong, H.; Shen, Z.; Lin, J.; Ruoff, R. S. Exploration of the Active Center Structure of Nitrogen-doped Graphene-based Catalysts for Oxygen Reduction Reaction. *Energy Environ. Sci.* **2012**, *5*, 7936−7942.
(43) Yang, Z.; Yao, Z.; Li, G.; Fang, G.; Nie, H.; Liu, Z.; Zhou, X.; Chen, X. A.; Huang, S. Sulfur-Doped Graphene as an Efficient Metal-free Cathode Catalyst for Oxygen Reduction. *ACS Nano* **2012**, *6*, 205−211.
(44) Xu, J.; Jang, K.; Choi, J.; Jin, J.; Park, J. H.; Kim, H. J.; Oh, D.-H.; Ahn, J. R.; Son, S. U. An Organometallic Approach for Ultrathin $SnO_xFe_yS_z$ Plates and Their Graphene Composites as Stable Anode Materials for High Performance Lithium Ion Batteries. *Chem. Commun.* **2012**, *48*, 6244−6246.
(45) Chang, S.-H.; Lu, M.-D.; Tung, Y.-L.; Tuan, H.-Y. Gram-Scale Synthesis of Catalytic Co_9S_8 Nanocrystal Ink as a Cathode Material for Spray-Deposited, Large-Area Dye-Sensitized Solar Cells. *ACS Nano* **2013**, *7*, 9443−9451.
(46) Sun, Y.; Liu, C.; Grauer, D. C.; Yano, J.; Long, J. R.; Yang, P.; Chang, C. J. Electrodeposited Cobalt-Sulfide Catalyst for Electrochemical and Photoelectrochemical Hydrogen Generation from Water. *J. Am. Chem. Soc.* **2013**, *135*, 17699−17702.
(47) Nørskov, J. K.; Rossmeisl, J.; Logadottir, A.; Lindqvist, L.; Kitchin, J. R.; Bligaard, T.; Jónsson, H. Origin of the Overpotential for Oxygen Reduction at a Fuel-Cell Cathode. *J. Phys. Chem. B* **2004**, *108*, 17886−17892.
(48) Ferrandon, M.; Kropf, A. J.; Myers, D. J.; Artyushkova, K.; Kramm, U.; Bogdanoff, P.; Wu, G.; Johnston, C. M.; Zelenay, P. Multitechnique Characterization of a Polyaniline-Iron-Carbon Oxygen Reduction Catalyst. *J. Phys. Chem. C* **2012**, *116*, 16001−16013.
(49) Gorlin, Y.; Lassalle-Kaiser, B.; Benck, J. D.; Gul, S.; Webb, S. M.; Yachandra, V. K.; Yano, J.; Jaramillo, T. F. In Situ X-ray Absorption Spectroscopy Investigation of a Bifunctional Manganese Oxide Catalyst with High Activity for Electrochemical Water Oxidation and Oxygen Reduction. *J. Am. Chem. Soc.* **2013**, *135*, 8525−8534.
(50) Shui, J.-L.; Karan, N. K.; Balasubramanian, M.; Li, S.-Y.; Liu, D.-J. Fe/N/C Composite in Li-O_2 Battery: Studies of Catalytic Structure and Activity toward Oxygen Evolution Reaction. *J. Am. Chem. Soc.* **2012**, *134*, 16654−16661.
(51) Landon, J.; Demeter, E.; İnoğlu, N.; Keturakis, C.; Wachs, I. E.; Vasić, R.; Frenkel, A. I.; Kitchin, J. R. Spectroscopic Characterization of Mixed Fe-Ni Oxide Electrocatalysts for the Oxygen Evolution Reaction in Alkaline Electrolytes. *ACS Catal.* **2012**, *2*, 1793−1801.
(52) Zong, C.; Zheng, L. R.; He, W.; Ren, X.; Jiang, C.; Lu, L. In Situ Formation of Phosphorescent Molecular Gold(I) Cluster in a Macroporous Polymer Film to Achieve Colorimetric Cyanide Sensing. *Anal. Chem.* **2014**, *86*, 1687−1692.
(53) Cao, B.; Veith, G. M.; Diaz, R. E.; Liu, J.; Stach, E. A.; Adzic, R. R.; Khalifah, P. G. Cobalt Molybdenum Oxynitrides: Synthesis, Structural Characterization, and Catalytic Activity for the Oxygen Reduction Reaction. *Angew. Chem., Int. Ed.* **2013**, *52*, 10753−10757.
(54) Risch, M.; Klingan, K.; Ringleb, F.; Chernev, P.; Zaharieva, I.; Fischer, A.; Dau, H. Water Oxidation by Electrodeposited Cobalt Oxides-Role of Anions and Redox-Inert Cations in Structure and Function of the Amorphous Catalyst. *ChemSusChem* **2012**, *5*, 542−549.
(55) Li, N.; Wang, X.; Derrouiche, S.; Haller, G. L.; Pfefferle, L. D. Role of Surface Cobalt Silicate in Single-Walled Carbon Nanotube Synthesis from Silica-Supported Cobalt Catalysts. *ACS Nano* **2010**, *4*, 1759−1767.
(56) Chen, W.-F.; Wang, C.-H.; Sasaki, K.; Marinkovic, N.; Xu, W.; Muckerman, J. T.; Zhu, Y.; Adzic, R. R. Highly Active and Durable Nanostructured Molybdenum Carbide Electrocatalysts for Hydrogen Production. *Energy Environ. Sci.* **2013**, *6*, 943−951.
(57) Chen, S.; Duan, J.; Jaroniec, M.; Qiao, S.-Z. Nitrogen and Oxygen Dual-Doped Carbon Hydrogel Film as a Substrate-Free Electrode for Highly Efficient Oxygen Evolution Reaction. *Adv. Mater.* **2014**, *26*, 2925−2930.
(58) Ma, T. Y.; Dai, S.; Jaroniec, M.; Qiao, S. Z. Metal-Organic Framework-Derived Hybrid Co_3O_4-Carbon Porous Nanowire Arrays as Reversible Oxygen Evolution Electrodes. *J. Am. Chem. Soc.* **2014**, *136*, 13925−13931.
(59) Ma, T. Y.; Dai, S.; Jaroniec, M.; Qiao, S. Z. Graphitic Carbon Nitride Nanosheet-Carbon Nanotube Three-Dimensional Porous Composites as High-Performance Oxygen Evolution Electrocatalysts. *Angew. Chem., Int. Ed.* **2014**, *53*, 7281−7285.
(60) Chen, S.; Qiao, S.-Z. Hierarchically Porous Nitrogen-Doped Graphene-$NiCo_2O_4$ Hybrid Paper as an Advanced Electrocatalytic Water-Splitting Material. *ACS Nano* **2013**, *7*, 10190−10196.
(61) Chen, S.; Duan, J.; Jaroniec, M.; Qiao, S. Z. Three-Dimensional N-Doped Graphene Hydrogel/NiCo Double Hydroxide Electrocatalysts for Highly Efficient Oxygen Evolution. *Angew. Chem., Int. Ed.* **2013**, *52*, 13567−13570.
(62) Gong, M.; Li, Y.; Wang, H.; Liang, Y.; Wu, J. Z.; Zhou, J.; Wang, J.; Regier, T.; Wei, F.; Dai, H. An Advanced Ni-Fe Layered Double Hydroxide Electrocatalyst for Water Oxidation. *J. Am. Chem. Soc.* **2013**, *135*, 8452−8455.
(63) Louie, M. W.; Bell, A. T. An Investigation of Thin-Film Ni-Fe Oxide Catalysts for the Electrochemical Evolution of Oxygen. *J. Am. Chem. Soc.* **2013**, *135*, 12329−12337.
(64) Zhang, Y.; Cui, B.; Qin, Z.; Lin, H.; Li, J. Hierarchical Wreath-like Au-$Co(OH)_2$ Microclusters for Water Oxidation at Neutral pH. *Nanoscale* **2013**, *5*, 6826−6833.
(65) Mahmood, N.; Zhang, C.; Jiang, J.; Liu, F.; Hou, Y. Multifunctional Co_3S_4/Graphene Composites for Lithium Ion Batteries and Oxygen Reduction Reaction. *Chem.—Eur. J.* **2013**, *19*, 5183−5190.
(66) Gu, Y.; Xu, Y.; Wang, Y. Graphene-Wrapped CoS Nanoparticles for High-Capacity Lithium-Ion Storage. *ACS Appl. Mater. Interfaces* **2013**, *5*, 801−806.
(67) Peng, S.; Li, L.; Li, C.; Tan, H.; Cai, R.; Yu, H.; Mhaisalkar, S.; Srinivasan, M.; Ramakrishna, S.; Yan, Q. In situ Growth of $NiCo_2S_4$ Nanosheets on Graphene for High-Performance Supercapacitors. *Chem. Commun.* **2013**, *49*, 10178−10180.
(68) Peng, S.; Li, L.; Tan, H.; Cai, R.; Shi, W.; Li, C.; Mhaisalkar, S. G.; Srinivasan, M.; Ramakrishna, S.; Yan, Q. MS_2 (M═Co and Ni) Hollow Spheres with Tunable Interiors for High-Performance Supercapacitors and Photovoltaics. *Adv. Funct. Mater.* **2014**, *24*, 2155−2162.
(69) Sohn, G.-J.; Choi, H.-J.; Jeon, I.-Y.; Chang, D. W.; Dai, L.; Baek, J.-B. Water-Dispersible, Sulfonated Hyperbranched Poly(ether-ketone) Grafted Multiwalled Carbon Nanotubes as Oxygen Reduction Catalysts. *ACS Nano* **2012**, *6*, 6345−6355.

DOI: 10.1021/am507033x
ACS Appl. Mater. Interfaces 2015, 7, 1207−1218